RSC Advances

ROYAL SOCIETY OF CHEMISTRY

www.rsc.org/advances

Pt-CeO_2/reduced graphene oxide nanocomposite for the electrooxidation of formic acid and formaldehyde

Biuck Habibi*, Nasrin Delnavaz

Electroanalytical Chemistry Laboratory, Department of Chemistry, Faculty of Sciences, Azarbaijan Shahid Madani University, Tabriz, Iran

*Corresponding author (Biuck Habibi). E-mail: B.Habibi@azaruniv.edu, biuckhabibi_a@yahoo.com and Tel & Fax: +98-41 34327541

Abstract

The Pt-CeO_2/reduced graphene oxide nanocomposite on the carbon-ceramic electrode (Pt-CeO_2/RGO/CCE) was prepared by a two-steps electrodeposition process. RGO was deposited on the CCE through a simple electrochemical method using graphene oxide and CCE as the precursor and electrode substrate, respectively. Then, RGO/CCE was used as a support for the Pt-CeO_2 nanoparticles deposition by another electrochemical process to form the nanocomposite based electrocatalyst; Pt-CeO_2/RGO/CCE. The obtained electrocatalyst was characterized by scanning electron microscopy, energy dispersive X-ray spectroscopy, X-ray diffraction and cyclic voltammetric techniques. The electrocatalytic activity of the Pt-CeO_2/RGO/CCE toward the oxidation of formic acid and formaldehyde was investigated by cyclic voltammetry and chronoamperometry in 0.1 M H_2SO_4 solution. It was found that the Pt-CeO_2/RGO/CCE is electrocatalytically more active than the Pt-CeO_2/CCE, Pt/RGO/CCE and Pt/CCE electrocatalysts. The increased electrocatalytic efficiency of Pt in Pt-CeO_2/RGO/CCE is likely to result from its combination with CeO_2 to form Pt-CeO_2 nanoparticles and their deposition on/in the RGO layers at the CCE surface. From the obtained results, it could be concluded that the Pt-CeO_2/RGO/CCE can be used as a potential and effective electrocatalyst for direct liquid fuel cell applications.

Keywords: Pt-CeO_2 nanoparticles, Reduced graphene oxide, Nanocomposite, Carbon-ceramic electrode, Formic acid, Formaldehyde.

1. Introduction

Tailoring of electrode surface with nanomaterials or nanocomposites is one of the attractive approaches in designing electrochemical interfaces for electrocatalysis of fuels oxidation in direct liquid fuel cells (DLFCs) [1, 2]. The nanostructured noble metals are of special interest in developing such interfaces owing to their unique electronic and electrocatalytic properties [3, 4]. At the same time, one of the main obstacles facing the development of the DLFCs via application of nanostructured noble metals as an anodic material is its sluggish kinetics caused by carbonaceous species poisoning effect. The intermediate carbonaceous products, such as carbon monoxide (CO), from the fuels oxidation over the noble metals surface are strongly adsorbed on the electrocatalyst surface and caused catalyst poisoning. On the other hand, noble metal nanostructures due to the high surface energy have a tendency to aggregate, which will decrease their surface area and result in a remarkable reduction in their performance. Meanwhile, the increasing request for noble metals and their finite availability in the nature cause them to be expensive. Consequently, it is desirable to explore simple and effective methods to prepare well-dispersed noble metal nanostructures with good size controllability to enhance the performance, tolerance against carbonaceous species and minimize the used amounts of noble metals. In practice, to solve the problem of poisoning effect, agglomeration and lower the usage of noble metals, an efficient strategy is to immobilize them along with different promoters in the form of alloy or conducting metal oxide/noble metal composite [5-7] at the nanosize particles in the inside or on the surface of solid supports with low cost, high surface area and superior chemical stability [8]. In fact, the electrocatalytic support retains the structure and morphology of the noble metal-based alloys or noble metal/metal oxide composites and exhibits a vital role in their swift performance and functionality**.** As mentioned above, to prevent the noble metal electrocatalysts such as Pt-based catalysts from being poisoned by carbonaceous species especially CO, besides the efforts to developing the noble metal-based alloys [9, 10], the recently developed strategy is synthesize the conducting metal oxide-based noble metal electrocatalysts via utilization of transition metal oxides [5]. Among the high surface area transition metal oxides, CeO_2, a material with fluorite structure in which the cation valence state can be switch between Ce^{+3} and Ce^{+4}, is of particular interest due to the high oxygen transfer ability, high efficiency for CO oxidation and much lower price, which might significantly promotes fuels oxidation and reduces the preparation cost of the electrocatalysts [6,

7, 11, 12]. Several researchers have reported different kinds of interaction between noble metals and CeO_2 and their effects on electrocatalytic activities [5-7, 11-14]. These studies have been shown that the nature and level of interaction depend on particular noble metal, electrocatalyst pretreatment, preparation technique, size of CeO_2 crystallite, lattice oxygen, and so on [13, 14].

On the other hand, practically in the electrocatalytic oxidation of fuels in DLFCs, the Pt-based electrocatalysts were supported on a carbonic substrate surface and always the supported electrocatalysts have shown higher electrocatalytic activities and utilization efficiencies than unsupported ones [13-15]. Nano dimensional carbonic materials such as carbon nanotubes, carbon nanofibers, carbon nanopowder, carbon dots and graphene not only have promising applications in many technological fields such as sensors [16], nanocomposites [17], batteries [18] and supercapacitors [19], because of their excellent physical and chemical properties, but also they have high potential applications as a heterogeneous catalyst support to dispersion and stabilization of the noble metal nanoparticles [20-23]. Graphene and its famous family, reduced graphene oxide (RGO), which can be considered as the unrolled carbon nanotubes, owing to their unique sheet structure, high mechanical stiffness, ultrahigh electron conductivity and extremely large surface area as well as superior thermal/chemical stability, are novel carbonic nanomaterials that have emerged as rapidly rising stars in the field of material science [23-33]. RGO which was produced through the reduction of graphene oxide displays a wrinkled structure due to the presence of lattice defects and provides a good platform to utilizes it [34-37] and its composites, hybrids and doped forms, which integrate the RGO with polymers, metal and metal oxides nanoparticles, nanotubes, fullerenes and etc., in various applications [30, 31, 38-42]. In this way, different nanocomposites and nanohybrids have been integrated with RGO or synthesized by using RGO as a template and were applied in different applications especially in electrocatalytic utilizations [36] such as sensors [34, 35, 43-46], biosensors [34, 35, 45, 47, 48], cathodic and anodic reactions in the fuel cells [38, 41, 45, 47, 49-54] and so on [45, 46, 53, 54].

In this work for the first time, we have prepared the Pt-CeO_2/RGO/CCE by a two-steps electrochemical procedure: (I) In the first step, the carbon-ceramic electrode (CCE), including interesting properties such as high porosity, conductivity, relative chemical inertness, good mechanical properties, physical rigidity and stability in various solvents [55-58], was coated by RGO via an electrochemical process. (II) In the second step, Pt-CeO_2 nanoparticles were deposited electrochemically on the RGO/CCE. After physiochemical characterization of the Pt-

CeO_2/RGO/CCE, its electrocatalytic activity toward the oxidation of formic acid and formaldehyde was evaluated by cyclic voltammetric and chronoamperometric techniques in 0.1 M H_2SO_4 solution and the obtained results were compared with those obtained at the Pt-CeO_2 and Pt modified carbon-ceramic electrode and also Pt/RGO/CCE. It was found that the Pt-CeO_2/RGO/CCE was electrocatalytically more active than them and had satisfactory stability and reproducibility when stored in ambient conditions or continues cycling. Consequently, the combination of the Pt-CeO_2 nanoparticles, RGO and carbon-ceramic substrate may lead to a nanocomposite material with improved electrocatalytic activities for application in DLFCs.

2. Experimental

2.1. Chemicals

Methyl trimethoxy silane (MTMOS), formic acid, formaldehyde, methanol, $H_2PtCl_6.6H_2O$, HCl, NaOH, H_2SO_4, $Ce(NO_3)_3.6H_2O$, graphite powder, Na_2HPO_4 and NaH_2PO_4 were purchased from Merck or Fluka and graphene oxide was synthesized from natural flake graphite by the Hummers method [59]. All solutions were prepared with double distilled water. Also all the experiments were carried out at room temperature.

2.2. Apparatus

The electrochemical experiments were carried out using an AUTOLABPGSTAT-30 (potentiostat/galvanostat) equipped with a USB electrochemical interface and a driven GEPS software was used for electrochemical experiments. A conventional three electrodes cell was used at room temperature. The Pt/CCE, Pt-CeO_2/CCE, Pt/RGO/CCE and Pt-CeO_2/RGO/CCE (3 mm diameter) were used as working electrodes. A saturated calomel electrode (SCE) and a platinum wire were used as the reference and auxiliary electrodes, respectively. JULABO thermostat was used to control cell temperature at 25°C. Scanning electron microscopy (SEM) and energy dispersive X-ray spectroscopy (EDX) were performed on a LEO 440i Oxford instrument. X-ray diffraction (XRD) of the nanocomposite was studied using a Brucker AXF (D8 Advance) X-ray power diffractometer with a Cu K_α radiation source (λ= 0.154056 nm) generated at 40 kV and 35 mA.

2.3. Preparation of the electrocatalysts

2.3.1. Preparation of the Pt-CeO_2/CCE

We have prepared the Pt-CeO_2 nanoparticles supported on the CCE by a two-steps procedure:

Step I: The sol-gel processing method was used for the fabricating of the CCE substrate according to the following procedure [57, 58]: The amount of 0.9 ml MTMOS was mixed with 0.6 ml methanol. After addition of 0.6 ml HCl 0.1 M as the catalyst, the mixture was magnetically stirred (for about 15 min) until producing a clear and homogeneous solution. Then, 0.3 g graphite powder was added and the mixture was stirred for other 5 minutes. Subsequently, the homogenized mixture was firmly packed into a Teflon tube (with 3 mm inner diameter and 10 mm length) and dried for at least 24 h at room temperature. A copper wire was inserted through the other end to set up electric contact. The electrode surface was polished with emery paper grade 1500 and rinsed with double distilled water.

Step II: 1g cerium (III) nitrate hexahydrate as a starting material was dissolved in 10 ml double distillated water [60, 61]. A solution of 0.15 M NaOH as the precipitating agent was added into the reaction mixture. The reaction solution was magnetically stirred to obtain CeO_2 nanoparticles by the homogeneous precipitation. Then, the solid product was filtered and washed with double distillated water and ethanol. Finally, the obtained precipitate was dried for at least 24 h at room temperature. The Pt-CeO_2 co-electrodeposition process was done in a 0.1 M H_2SO_4 continuous stirring solution containing an excess amount of CeO_2 particles as a suspension and 1×10^{-3} M of $H_2PtCl_6.6H_2O$. The Pt-CeO_2 nanoparticles were electrodeposited on the CCE at a constant potential of -0.3 V vs. SCE. In this process, which is known as the ‘‘occlusion electrodeposition’’ method for the deposition of metal together with an oxide on the surface of a substrate [61, 62], the Pt nanoparticles ($PtCl_6^{-2} + 4e^- \rightarrow Pt + 6Cl^-$) assimilate the CeO_2 particles during film growth to obtain the final modified electrode, Pt-CeO_2/CCE. The electrodeposited mass of Pt in Pt-CeO_2/CCE can be calculated by integration of the electrical charge consumed during the electrodeposition process: Q_{Pt}= 0.0277 C and assuming, 100% current efficiency, the quantity of electrodeposited Pt (W_{Pt}) was obtained ($W_{Pt} = Q_{dep}$ M/ zF) to be 0.02 mg/cm^2. It should be noted that, by passing the same electrical charge in preparation process of other electrocatalysts; Pt/RGO/CCE, Pt/CCE and Pt-CeO_2/RGO/CCE, the amount of Pt in all electrocatalysts will be the same: 0.02 mg/cm^2.

2.3.2. Preparation of the Pt-CeO_2/RGO/CCE

The CCE was prepared according to the above-mentioned process. Graphene oxide was synthesized from natural flake graphite by the Hummers method [59]. The obtained graphene oxide powder was exfoliated in a 0.07 M phosphate buffer solution (pH 8.5) by ultrasonication to form a colloidal dispersion of 1.0 mg ml^{-1} graphene oxide. Then, the polished CCE was immersed into the graphene oxide colloid and its potential was swept from (-1.5 to 0.5 V) for about 8-10 cycles at scan rate of 20 mV s^{-1}. Fig. 1 shows the eight continues cyclic voltammograms (CVs) during the electrolysis process of graphene oxide at the CCE, where one anodic peak (a_1 at about -0.3 V) and two cathodic peaks [c_1 at about -0.5 V and c_2 at about -1.0 V] are observed during the electrodeposition process [inset of Fig.1 shows the CV of CCE in the phosphate buffer solution (0.07 M and pH 8.5) without graphene oxide at scan rate of 20 mV s^{-1}]. In the first CV, the reduction peak (c_2) at around to -1.0 V is due to the electrochemical reduction of graphene oxide [63] on the CCE. By increasing the potential cycling, the current of this cathodic peak, c_2, increases firstly (until 10 cycles), then decreases and finally disappears as the potential cycling proceeds (›15 cycles). When the c_2 cathodic peak disappears, the electrochemical reduction of graphene oxide is considered to be completed (however there are still some oxygen-containing groups such as carboxylic and hydroxide groups on RGO which are too stable under electrochemical conditions) [63, 64]. On the other hand, continues increase of the peak currents (a_1 and c_1) with successive potential cycling indicates that the electrodeposition of RGO film on the CCE has been progressed and completed after 10 cycles [63-65]: the requested substrate, RGO/CCE, was achieved. It should be noted that, the CV of the RGO/CCE in the phosphate buffer solution shows only peaks a_1 and c_1 (not shown). Therefore, the cathodic peak, c_2, is undoubtedly attributed to the irreversible electrochemical reduction of graphene oxide [63-65] and the anodic peak, a_1, and its cathodic pair, c_1, are attributed to quasi-reversible redox couple of RGO on the CCE. The obtained RGO/CCE was washed with double distilled water and then dried it in air. The Pt-CeO_2 nanoparticles were electrodeposited on the RGO/CCE from a 0.1 M H_2SO_4 continuous stirring solution containing an excess amount of CeO_2 particles as a suspension and 1×10^{-3} M of $H_2PtCl_6.6H_2O$. During the electrodeposition, the CeO_2 particles in a suspension promoted by magnetic stirring and $PtCl_6^{-2}$ ions together with its particles are dragged toward the RGO/CCE surface. As mentioned above, the idea is that the metal ions

assimilate the CeO_2 particles during film growth to obtain the requested Pt-CeO_2 nanocomposite modified RGO/CCE: Pt-CeO_2/RGO/CCE [61, 62].

3. Results and discussion

3.1. Physical characteristics of the Pt-CeO_2/RGO/CCE electrocatalyst

In order to perform surface characterization of the Pt-CeO_2/RGO/CCE electrocatalyst and comparison studies, the surface morphology of the bare CCE, RGO/CCE, CeO_2/RGO/CCE, Pt/RGO/CCE, Pt-CeO_2/CCE and Pt-CeO_2/RGO/CCE was investigated by SEM and corresponding results are shown in Fig. 2. Fig. 2A shows the structure of the bare CCE surface immediately after polishing with emery paper, grade 1500. As seen in this image, the surface of bare CCE is dense and scaly. Fig. 2B shows the SEM image of the RGO/CCE surface. As can be seen, the surface of CCE is completely protected with RGO layers and layer structure of the RGO is favorable and ready for immobilization of compounds or dispersion and electrodeposition of metal nanoparticles. After co-deposition of the Pt-CeO_2 nanoparticles on the RGO/CCE surface (Fig. 2C), flower like of Pt-CeO_2 nanoparticles are appeared on the RGO/CCE. It seems, the flower like structures of Pt-CeO_2 nanoparticles are not the individual Pt-CeO_2 crystallites. Probably, they are collections, like as a flower, consisting of crystallite aggregates. Fig. 2, images D, and E show the surface of the Pt-CeO_2/CCE and Pt/RGO/CCE, respectively. As can be seen, the surface morphology of these modified electrodes is completely different in comparison with Pt-CeO_2/RGO/CCE surface. The Pt-CeO_2 nanoparticles in the Pt-CeO_2/RGO/CCE are smaller and have distinct shapes than those in the Pt-CeO_2/CCE and Pt/RGO/CCE, which may suggest that the former have more active sites and should have better electrocatalytic activity. On the other hand, as reported in the literature [42], among the various shapes, nanostructures with branched morphology such as flower shaped (like as image C) and dendritic structures are of particular interest. These materials not only show maximum electrocatalytic performance by their high specific surface area but also utilize fully their intrinsic capability because of the presence of highly reactive edges, corners and stepped atoms on their branches. Finally, Fig. 2F shows the surface morphology of the CeO_2/RGO/CCE. As can be seen, the surface of the CeO_2/RGO/CCE is very similar to the surface of RGO/CCE; just like its previous surface. Indeed it seems that any additional particles aren't electrodeposited on its surface.

Furthermore, the EDX analysis of the Pt-CeO_2/RGO/CCE in Fig. 3 and Pt/RGO/CCE, CeO_2/RGO/CCE and RGO/CCE (inset a, b and c, respectively) detected Pt, Ce, O, Si (from MTMOS) and C atoms. Combining the facts of the crystal plane formation (XRD results) and a large amount of Pt and Ce detected in Fig. 3, it can be inferred that the nanoparticles mainly consist of Pt and CeO_2. The spectrum in inset a, corresponds to the Pt/RGO/CCE, shows only Pt along with other common atoms. The EDX spectra of the CeO_2/RGO/CCE (inset b) and similarly the RGO/CCE (inset c) contain only strong peaks for C, Si and O elements, suggesting that the CeO_2 particles aren't present on them. These results are in agreement with the obtained SEM images and indicate that in the absence of the $PtCl_6^{-2}$ ions at the occlusion electrodeposition process, the CeO_2 particles couldn't deposit on the surface of the RGO/CCE.

The crystallographic structure and chemical phase composition of the electrocatalysts were determined by XRD patterns. Fig. 4 shows the XRD patterns of the Pt/RGO/CCE (A) and Pt-CeO_2/RGO/CCE (B). The peaks at 2θ values of 26.96° and 55° in both XRD patterns correspond to the supporting carbonic material (graphite powder) (002) and (006), respectively. Also, a broad peak at 2θ value of about 23.32° in both XRD patterns corresponds to (002) graphitic peak of RGO [63, 66]. Appearance of the broad diffraction peak at 2θ values of 23.32° in the XRD patterns of both electrocatalysts gives evidence that the graphite oxide was reduced to RGO at the surface of CCE [66]. XRD pattern of the Pt/RGO/CCE exhibits the characteristic diffraction peaks of Pt (111), (200), (220), (311) and (222) at 2θ values of 40.08°, 46.8°, 67.88°, 83.76° and 87.24°, respectively [67]. For the Pt-CeO_2/RGO/CCE the main characteristic peaks at 40.4° (111), 46.6° (200), 68.27° (220), 83.84° (311) 87.28° (222) for Pt and at 57.04° (331), 60.24° (222), 77.92° (420) for CeO_2 are observed [13, 68]. As seen, no shift at the position of Pt diffraction peaks was observed which indicate that adding of the CeO_2, has no effect on the crystallographic structure of the Pt nanoparticles. Using the Scherrer equation [69]; $D_c = 0.9\ \lambda/\beta \cos\theta$ (where $\lambda = 0.154056$ nm, β is the full width at half-maximum in radians and θ is the peak position in degrees), the average crystallite size (D_c) of Pt and CeO_2 nanoparticles is estimated to be 25 nm and 95 nm, respectively [60, 70].

3.2. Electrochemical characteristics of the Pt-CeO_2 /RGO/CCE electrocatalyst

The electrochemical behavior of the Pt-CeO_2/RGO/CCE and also Pt-CeO_2/CCE for comparison was investigated using cyclic voltammetry at a scan rate of 50 mV s^{-1} in 0.1 M

H_2SO_4 aqueous solution within the potential range of -0.3 and 1.3 V. Fig. 5 shows the CVs of the Pt-CeO_2/RGO/CCE (black line) and Pt-CeO_2/CCE (dashed line). The Pt-peaks for the hydrogen under potential deposition (H_{upd}), the oxidation of hydrogen (H_{oh}), formation of Pt oxides (a_1) and their reduction (a_2) are present in the CVs of the Pt-CeO_2/RGO/CCE and Pt-CeO_2/CCE electrocatalysts but they become ill-shaped compared with Pt/CCE [57].

The actual active surface area (A_r) of the Pt-based electrocatalyst is equivalent to the number of Pt sites available for hydrogen adsorption/desorption [71]. The A_r of co-electrodeposited Pt-CeO_2 nanoparticles was estimated from the hydrogen adsorption peaks [hydrogen under potential deposition (H_{upd})] on CV according to $A_r = Q_H/Q_0$, where Q_H is the electric charge related to hydrogen adsorption on the Pt-CeO_2/RGO/CCE and Q_0 is the theoretical charge required to reduce a monolayer of hydrogen on the Pt atoms. Integration of charge in the potential ranges of -300 to -30 mV in Fig. 5, black line, allows to estimates the Q_H (μC), due to the hydrogen adsorption. For evaluation of the A_r, an assumption must be made about the atoms on the electrocatalyst surface which are accessible to hydrogen adsorption; assuming one H_{ad} per Pt surface atom, the theoretical charge associated with a monolayer of hydrogen formed on the bases of: $H^+ + e^- \rightarrow H_{ad}$, Q_0, was estimated to be 210 μC/real cm^2 as follows: Q_0(μC)/real cm^2= F×n/N, where n is the number of platinum atoms ($1.3 \times 10^{15}/cm^2$) and N is Avogadro constant [55, 56]. Form the obtained Q_H and the theoretical charge, Q_0, A_r of the Pt-CeO_2/RGO/CCE was calculated to be 1.41 cm^2. The specific surface area, S (in $m^2\ g^{-1}$), of the Pt-CeO_2/RGO/CCE electrocatalyst was also estimated as follows [30]: $S=100A_r/(WA_g)=10.07$ [A_g: geometric surface area=0.07 cm^2, W (in μg cm^{-2}): amount of loaded platinum]. On the other hand, assuming spherical particles with similar radius, the average particle size of the Pt nanoparticles in the Pt-CeO_2/RGO/CCE electrocatalyst, d, can be calculated from the following equation using the Gloaguen and et al. method [72]: $d=6000/(\rho S)$, where d is the average particle size of the Pt nanoparticles in nm, ρ is the density of Pt (ρ=21.4 g cm^{-3}) and S is the specific surface area (10.07 $m^2\ g^{-1}$) of the Pt nanoparticles. The average particle size of Pt nanoparticles in the Pt-CeO_2/RGO/CCE was calculated to be d=27.84 nm which is in good agreement with the average particle size obtained for XRD result using Scherrer equation.

3.3. Electrocatalytic activity of the Pt-CeO_2/RGO/CCE toward the oxidation of formic acid and formaldehyde

The electrocatalytic activity of the Pt-CeO_2/RGO/CCE toward the oxidation of formic acid and formaldehyde were evaluated by cyclic voltammetry. Fig. 6 shows the CV of the Pt-CeO_2/RGO/CCE in a 0.1 M H_2SO_4 solution + 0.1 M formic acid. For comparison, the CVs of the Pt-CeO_2/CCE (inset A), Pt/RGO/CCE (inset B), Pt/CCE (inset C) [55], CeO_2/RGO/CCE and RGO/CCE (inset D, curve1 and 2, respectively) in the same conditions are shown in Fig. 6. It can be seen from the CV of formic acid on the Pt-CeO_2/RGO/CCE that the reaction commences in the hydrogen adsorption/desorption region, proceeds slowly in the positive direction and then reaches a plateau. At potentials more than ca. 0.5 V, the reaction becomes accelerated and maximum rate occurs at ca. 0.86 V. An increase in the current at potentials more than ca. 1.1 V is assigned to oxygen evolution. Upon reversing the potential sweep, a very steep increase courses in the current at ca. 0.48 V and a maximum current is observed at ca. 0.36 V. After that, the current gradually decreases but the reaction rate is still faster than in the forward scan. This anodic peak in the reverse scan is attributed to the removal of the incompletely oxidized carbonaceous species formed in the forward scan [73]. As evidenced in Fig. 6 and its insets, the Pt-CeO_2/RGO/CCE electrocatalyst exhibits a much higher anodic peak current density for formic acid oxidation than the Pt-CeO_2/CCE (inset A), Pt/RGO/CCE (inset B) and Pt/CCE (inset C) in the forward scan. The anodic peak current density at the Pt-CeO_2/RGO/CCE is about 60.1 mA cm^{-2}, while it is 51.8 mA cm^{-2} at the Pt-CeO_2/CCE, 46.2 mA cm^{-2} at the Pt/RGO/CCE and 6.6 mA cm^{-2} at the Pt/CCE electrocatalysts. This indicates that the incorporation of Pt nanoparticles along with CeO_2, Pt-CeO_2, supported on the RGO greatly enhanced the utilization of Pt nanoparticles in the electrooxidation of formic acid. Moreover, the ratio of the anodic peak current density in the forward scan (J_f) to the anodic peak current density in the backward scan (J_b) can be used to evaluate the electrocatalyst tolerance to the intermediate carbonaceous species which formed in the electrooxidation reaction and accumulated on electrocatalyst surface [55]. The higher J_f/J_b value indicates higher tolerance to intermediate carbonaceous species which means formic acid can be oxidized to final product much more efficiently. The ratio of J_f/J_b for formic acid electrooxidation on the Pt-CeO_2/RGO/CCE is calculated to be 1.14, while for the Pt-CeO_2/CCE, Pt/RGO/CCE and Pt/CCE electrocatalysts are 1.13, 1.31 and 0.49, respectively, which suggests that Pt-CeO_2/RGO/CCE has less carbonaceous accumulation and hence is more

tolerant toward CO poisoning especially in comparison with Pt/CCE (J_f/J_b =0.49). The results of the electrochemical parameters of formic acid oxidation at the present electrocatalysts were summarized in Table 1. As can be seen in Table 1, the onset potential for the oxidation of formic acid at the Pt-CeO_2/RGO/CCE electrocatalyst is about -0.20 V, which shifts negatively about 100-200 mV compared to that at the Pt-CeO_2/CCE, Pt/RGO/CCE and Pt/CCE electrocatalysts. The fact that the electrooxidation of formic acid taking place at lower potential with higher J_f/J_b value and lower onset potential discloses that the Pt-CeO_2/RGO/CCE electrocatalyst exhibits a higher electrocatalytic activity for the electrooxidation of formic acid than that of the others. The significant enhancement in the electrocatalytic activity of the Pt-CeO_2/RGO/CCE as compared with Pt-CeO_2/CCE, Pt/RGO/CCEB and Pt/CCE electrocatalysts can be attributed to two factors:

First: the role of the RGO in the improvement of the catalytic performances of the Pt-CeO_2/RGO/CCE electrocatalyst. The role of RGO can also be explained by two facts: (I) the role of the RGO as a support in well, uniform and smaller distribution of the Pt-CeO_2 nanoparticles and (II) possible bifunctional effect between the remaining oxygenated groups on the ORG and Pt-CeO_2 nanoparticles similar with the commonly accepted bifunctional effect between Pt and Ru [26, 74]. As can be found in the literature [74, 75], oxygen-containing groups on the RGO can improve the electrocatalytic activity of Pt nanoparticles slightly by playing the role of ruthenium in the case of Pt-Ru electrocatalyst [75] to remove the intermediate carbonaceous species and contribute to the low poisoning. On the other hand, the remaining functional groups like as carboxylic and hydroxide groups on the RGO (incomplete reduction) may be responsible for improved tolerance to CO observed in the Pt-CeO_2/RGO/CCE electrocatalyst [26].

Second: the synergistic effects between the Pt nanoparticles and CeO_2 [7, 68, 70]. The improvement of the electrooxidation performances as assisted by CeO_2 can be described by two probabilities [13]: (I) Chemical enhancement of the electrooxidation of the adsorbed CO as supported by CeO_2 as an oxygen donor, or by the effect of CeO_2's altering the electrocatalyst's surface morphology (as can be seen in the SEM images), physically preventing the CO adsorption. The probable mechanism for this proposes can be described by the following reactions [13, 76]:

$$Pt\text{-}CO_{ads} + 4CeO_2 + 2H^+ + 2e^- \leftrightarrow 2Ce_2O_3 + Pt + CO_2 + H_2O \quad (1)$$

$$4CeO_2 + 4H^+ + 4e^- \leftrightarrow 2Ce_2O_3 + 2H_2O \quad (2)$$

which assist on the weakening of the Pt-CO bond, thus reducing the CO poisoning effect and promoting the electrooxidation of the formic acid. (II) A second possible mechanism for CeO_2's proposed improvement of the electrooxidation of formic acid can be explained by the bifunctional mechanism; the OH_{ads} species on metal oxide can transform CO_{ads} on the Pt nanoparticles to CO_2, releasing the active sites on Pt nanoparticles for further electrochemical reaction [70, 77, 78].

$$CeO_2 + H_2O \leftrightarrow CeO_2{-}OH_{ads} + H^+ + e^- \quad (3)$$

$$Pt{-}CO_{ads} + CeO_2{-}OH_{ads} \leftrightarrow Pt + CeO_2 + CO_2 + H^+ + e^- \quad (4)$$

On the other hand, the combination of Pt and CeO_2 could assists the oxidation of the adsorbed intermediated, CO_{ads}, according to the bifunctional mechanism, where the OH_{ad} species could form on the surface of the CeO_2 and could transform CO_{ads} on the surface of Pt nanoparticles to CO_2, which release the active sites of the Pt nanoparticles for contribution in main electrooxidation reactions. All these results demonstrate that the Pt-CeO_2/RGO/CCE in the electrooxidation of formic acid is more active than the Pt-CeO_2/CCE, Pt/RGO/CCE, Pt/CCE [57, 70, 79-81].

Moreover, comparison of the obtained results in the electrooxidation of formic acid on the Pt-CeO_2/CCE and Pt/RGO/CCE show that the effects of CeO_2 in the improvement of the electrocatalytic activity of Pt nanoparticles is much higher than the RGO effects. As reported in the literature [68], CeO_2 has been generally used as a kind of oxygen reservoir to regulate the oxygen species on the electrocatalysts surface [82]. CeO_2 has a fluorite structure whose cations can switch between oxidation states (Ce^{+3}/Ce^{+4}) (Eq.s 2, 3), and consequently has the ability to act as an oxygen species buffer [68]. Therefore, introduction of CeO_2 into the electrocatalyst improves the dispersion of the Pt nanoparticles and consequently increasing the proportion of Pt exposed to oxygen. On the other hand, CeO_2 provides a good situation for oxygen transport through valence variation, so that the CeO_2 synergism with Pt effectively promotes the oxygen reduction reaction [68, 83, 84]. These results indicate that the oxygenated Pt species have a weaker adsorption energy on the surface of the Pt-CeO_2/CCE electrocatalyst than on the surface of the Pt/RGO/CCE electrocatalyst, which means that the desorption of oxygenated Pt species is easier on the Pt-CeO_2/CCE than on the Pt/RGO/CCE [5].

Inset D in Fig. 6 shows the CVs of the CeO_2/RGO/CCE and RGO/CCE in a 0.1 M H_2SO_4 solution + 0.1 M formic acid. It can be seen, there is no anodic peak corresponds to the formic acid oxidation on the CeO_2/RGO/CCE (curve 1) and RGO/CCE (curve 2) [68], indicating that the RGO and CeO_2/RGO have no electrocatalytic activity toward formic acid oxidation.

Fig. 7 shows the CV of the Pt-CeO_2/RGO/CCE electrocatalyst in a solution of 0.1 M H_2SO_4 + 0.1 M formaldehyde. For comparison, the CVs of the Pt-CeO_2/CCE (inset A), Pt/RGO/CCE (inset B), Pt/CCE (inset C) [57] and CeO_2/RGO/CCE and RGO/CCE (inset D, curve1 and 2, respectively) were also shown in that. As can be seen in Fig. 7, the electrochemical behavior of formaldehyde is similar to formic acid electrooxidation at the same electrocatalysts: One main oxidation peak in the forward scan at all electrocatalysts which is located at potentials between 0.7 V - 0.9 V with peak current density corresponds to the type and performance of the studied electrocatalysts and one main oxidation peak in the backward scan. CV responses reveal that the Pt-CeO_2/RGO/CCE has higher electrocatalytic activity in the electrooxidation of formaldehyde than the others electrocatalysts. The electrochemical parameters of formaldehyde electrooxidation at the present electrocatalysts were summarized in Table 1. As can be seen in Table 1, the Pt-CeO_2/RGO/CCE exhibits a higher electrocatalytic activity in the electrooxidation of formaldehyde than that of the others.

Inset D in Fig. 7 shows that the CeO_2/RGO/CCE (curve 1) and RGO/CCE (curve 2) have no electrocatalytic activity toward formaldehyde electrooxidation [68].

Finally, to compare the electrocatalytic performance of Pt-CeO_2/RGO/CCE toward formic acid and formaldehyde oxidation with other electrocatalysts in same conditions, the electrochemical parameters in oxidation of formic acid and formaldehyde (E_{onset}, E_{pf}, E_{pb}, I_{pf}, I_{pb}, I_{pf}/I_{pb} and also the stability of the electrocatalysts) obtained in this work and others studies were listed in Table 2. Table 2 shows that the Pt-CeO_2/RGO/CCE exhibits better or comparable electrocatalytic performance than other reported electrocatalysts toward formic acid and formaldehyde oxidation. These results confirmed that the Pt-CeO_2/RGO/CCE exhibits a promising catalytic behavior toward formic acid and formaldehyde oxidation and demonstrate that Pt-CeO_2 nanoparticles by providing a flower like nanostructure on the RGO/CCE and reducing the loading of expensive noble metals improve Pt utilization efficiency.

A further investigation was done to find out the transport characteristics of formic acid and formaldehyde on the Pt-CeO_2/RGO/CCE electrocatalyst. The influence of the scan rate (v)

on the electrooxidation of formic acid and formaldehyde at the Pt-CeO_2/RGO/CCE was investigated and shown in Fig. 8 (A) and (B), respectively. The results show that the currents associated to the formic acid and formaldehyde electrooxidation increase with scan rate. The anodic peak current densities in the forward scan are linearly proportional to $v^{1/2}$, as shown in inset of (I) in Fig. 8 A and (I') in Fig. 8 B, suggest that the electrocatalytic oxidation reactions of formic acid and formaldehyde on the Pt-CeO_2/RGO/CCE are diffusion-controlled processes. Also, as can be seen in insets (II) and (II') of Fig. 8 (A) and (B), respectively, the potentials of anodic peaks in the forward scan (curve a_1 and a'_1) shift to high potentials with increasing of the scan rate [99]. Whereas, the potentials of cathodic peaks (c_1 and c'_1 for formic acid and formaldehyde, respectively) and anodic peak (a_2 and a'_2 for formic acid and formaldehyde, respectively) in the backward scan shift to higher positive potentials with increasing of the scan rate. These results indicate that the electrooxidation of formic acid and formaldehyde and also the process in the cathodic reaction at the Pt-CeO_2/RGO/CCE are irreversible electrode processes.

In order to evaluate the capacity of the Pt-CeO_2/RGO/CCE in the electrooxidation of formic acid and formaldehyde, the effect of fuels concentrations on the corresponding anodic peaks currents was investigated by CV. According to experimental data, the anodic peak current density of formic acid and formaldehyde increased by their concentrations, and reached to the nearly constant values for concentrations higher than 1.5 M and 1.2 M for formic acid and formaldehyde, respectively. We assume this effect caused by saturation of active sites at the surface of Pt-CeO_2/RGO/CCE electrocatalyst [100].

3.4. Long-term stability of the Pt-CeO_2/RGO/CCE electrocatalyst

Practically, long-term stability of the anodic material in the fuel cells is important. The long-term activity and durability of the Pt-CeO_2/RGO/CCE and Pt-CeO_2/CCE electrocatalysts were assessed by chronoamperometry tests. Fig. 9 shows the typical chronoamperometric response curves of 0.1 M formic acid (A) and 0.1 M formaldehyde (B) in 0.1 M H_2SO_4 on the Pt-CeO_2/RGO/CCE and Pt-CeO_2/CCE electrocatalysts under a constant potential of 0.85 V for formic acid and 0.9 V for formaldehyde for 800 s. It was found that the currents observed from chronoamperograms were in good agreement with the currents observed from CVs and show that the both electrocatalysts have significantly stability toward formic acid and formaldehyde

electrooxidation. The long-term stability of the Pt-CeO_2/RGO/CCE and Pt-CeO_2/CCE electrocatalysts was further examined in 0.1 M H_2SO_4 solution containing 0.1 M formic acid (Fig. 10A) and 0.1 M formaldehyde (Fig. 10B) by CV in consecutive scans. It can be observed from Fig. 10A that the anodic peak current density remains constant with an increase in the scan number at the initial stage. By increasing in the number of scans the anodic peak current densities gradually decrease. In general, the loss of the catalytic activity after successive number of scans may result from the consumption of formic acid during the CV scan. It may also be due to poisoning and the structure change of the Pt-CeO_2 nanoparticles as a result of the perturbation of the potentials during the scanning in aqueous solutions. After the long-term cyclic voltammetry experiments, the Pt-CeO_2/RGO/CCE was stored in water for a week and then the formic acid oxidation was carried out again by the CV. This process revealed that the excellent electrocatalytic activity the formic acid oxidation was still observable. Similar behavior was obtained for formaldehyde oxidation in continues cycling (Fig. 10B) and stability study [57, 79].

4. Conclusions

Pt-CeO_2/RGO/CCE electrocatalyst was successfully fabricated by a simple two-steps electrochemical deposition process consisting: step I; electrodeposition of the RGO on the CCE through a simple electrochemical process using graphene oxide and CCE as the precursor and electrode substrate, respectively and step II; co-electrodeposition of the Pt-CeO_2 nanoparticles on the RGO/CCE by using another electrochemical process. The obtained Pt-CeO_2/RGO/CCE electrocatalyst was characterized by SEM, EDX, XRD and electrochemical methods. Then, the electrocatalytic performances of the Pt-CeO_2/RGO/CCE toward the oxidation of formic acid and formaldehyde were investigated by cyclic voltammetric and chronoamperometric methods. Compared with Pt/RGO/CCE, Pt-CeO_2/CCE and Pt/CCE, Pt-CeO_2/RGO/CCE electrocatalyst exhibited higher catalytic activity for formic acid and formaldehyde oxidation. The significant enhancement in the catalytic activity of the Pt-CeO_2/RGO/CCE electrocatalyst as compared with Pt-CeO_2/CCE, Pt/RGO/CCE and Pt/CCE electrocatalysts may be attributed to: the role of the RGO in the increased performances of Pt-CeO_2 nanoparticles and the synergistic effects between the Pt nanoparticles and CeO_2 nanoparticles in the enhanced catalytic performances of the Pt-CeO_2/RGO/CCE electrocatalyst.

Acknowledgment

The authors are grateful to the research office of Azarbaijan Shahid Madani University for its financial support.

References

[1] S. Basri, S.K. Kamarudin, W.R.W. Daud and Z. Yaakub, Int. J. Hydrogen Energy, 2010, **35** ,7957.

[2] Y. Qiao and C.M. Li, J. Mater. Chem., 2011, **21**, 4027.

[3] H. Liu, C. Song, L. Zhang, J. Zhang, H. Wang and D.P. Wilkinson, J. Power Sources, 2006, **155**, 95.

[4] S. Guo and E. Wang, Nano Today, 2011, **6**, 240.

[5] M.A. Scibioh, S.K. Kim, E.A. Cho, T.H. Lim, S.A. Hong and H.Y. Ha, Appl. Catal. B Environ, 2008, **84**, 773.

[6] Y.Y. Chu, Z.B. Wang, Z.Z. Jiang, D.M. Gu and G.P. Yi, Adv. Mater., 2011, **23**, 3100.

[7] L. Yu and J. Xi, Int. J. Hydrogen Energy, 2012, 37, 15938.

[8] M. Yaldagard, M. Jahanshahi and N. Seghatoleslami, World J. Nano. Sci. Eng., 2013, **3**, 121.

[9] W. Zhou, Z. Zhou, S. Song, W. Li, G. Sun, P. Tsiakaras and Q. Xin, Appl. Catal. B Environ, 2003, **46**, 273.

[10] C. Lamy, E.M. Belgsir and J-M. Léger, J. Appl. Electrochem., 2001, **31**, 799.

[11] J.W. Guo, T.S. Zhao, J. Prabhuram, R. Chen and C.W. Wong, J. Power Sources, 2006, **156**, 345.

[12] A. Altamirano-Gutiérrez, A.M. Fernández and F.J. Rodríguez Varela, Int. J. Hydrogen Energy, 2013, **38**, 12657.

[13] D.J. Guo and Z.H. Jing, J. Power Sources, 2010, **195**, 3802.

[14] N. Chakroune, G. Viau, S. Ammar, L. Poul, D. Veautier, M.M. Chehimi, C. Mangeney, F. Villain and F. Fiévet, Langmuir, 2005, **21**, 6788.

[15] X. Yu and P.G. Pickup, J. Power Sources, 2008, **182**, 124.

[16] Q. Zhao, Z. Gan and Q. Zhuang, Electroanalysis, 2002, **14**, 1609.

[17] M. Baibarac and P. Gómez-Romero, J. Nanosci. Nanotechnol., 2006, **6**, 289.

[18] L.L. Zhang and X.S. Zhao, Chem. Soc. Rev., 2009, **38**, 2520.

[19] S. Bose, T. Kuila, A.K. Mishra, R. Rajasekar, N.H. Kim and J.H. Lee, J. Mater. Chem., 2012, **22**, 767.

[20] J. Prabhuram, T.S. Zhao, Z. K. Tang, R. Chen and Z.X. Liang, J. Phys. Chem. B, 2006, **110,** 5245.

[21] J. Guo, G. Sun, Q. Wang, G. Wang, Z. Zhou, S. Tang, L. Jiang, B. Zhou and Q. Xin, Carbon, 2006, **44**, 152.

[22] Z. Liu, L.M. Gan, L. Hong, W. Chen and J.Y. Lee, J. Power Sources, 2005, **139**, 73.

[23] C. Venkateswara Rao, C.R. Cabrera and Y. Ishikawa, J. Phys. Chem. C, 2011, **115**, 21963.

[24] X. Huang, X.Y. Qi, F. Boey and H. Zhang, Chem. Soc. Rev., 2012, **41**, 666.

[25] C. Xu, X. Wang and J. Zhu, J. Phys. Chem. C, 2008, **112**, 19841.

[26] Y. Li, W. Gao, L. Ci, C. Wang and P.M. Ajayan, Carbon, 2010, **48**, 1124.

[27] X. Zhou, X. Huang, X. Qi, S. Wu, C. Xue, F.Y.C. Boey, Q. Yan, P. Chen and H. Zhang, J. Phys. Chem. C, 2009, **113**, 10842.

[28] Z. Huang, H. Zhou, C. Li, F. Zeng, C. Fua and Y. Kuang, J. Mater. Chem., 2012, **22**, 1781.

[29] Z. Ji, X. Shen, Y. Xu, G. Zhu and K. Chen, J. Colloid Interface Sci., 2014, **432**, 57.

[30] C.N.R. Rao, A.K. Sood, K.S. Subrahmanyam, and A. Govindaraj, Angew. Chem. Int. Ed., 2009, **48**, 7752.

[31] C. Soldano, A. Mahmood and E. Dujardin, Carbon, 2010, **48**, 2127.

[32] M.J. Allen, V.C. Tung, and R.B. Kaner, Chem. Rev., 2010, **110**, 132.

[33] Y. Zhu, S. Murali, W. Cai, X. Li, J.W. Suk, J.R. Potts and R.S. Ruoff, Adv. Mater., 2010, **22**, 3906.

[34] Y. Shao, J. Wang, H. Wu, J. Liu, I.A. Aksay, and Y. Lin, Electroanalysis, 2010, **22**, 1027.

[35] M. Zhou, Y. Zhai, and S. Dong, Anal. Chem., 2009, **81**, 5603.

[36] D.A.C. Brownson and C.E. Banks, Analyst**,** 2010,**135**, 2768.

[37] M. Pumera, Electrochem. Commun., 2013, **36**, 14.

[38] C. Xu , X. Wang and J. Zhu, J. Phys. Chem. C, 2008, **112**, 19841.

[39] S.Stankovich, D.A. Dikin, G.H.B. Dommett, K.M. Kohlhaas, E.J. Zimney, E.A. Stach, R.D. Piner, S.T. Nguyen and R.S. Ruoff, Nature, 2006, **442**, 282.

[40] X. Zhou, X. Huang, X. Qi, S. Wu, C. Xue, F.Y.C. Boey, Q. Yan, P. Chen and H. Zhang, J. Phys. Chem. C, 2009, **113**, 10842.

[41] Y. Zhang, K. Fugane, T. Mori, L. Niu and J. Ye, J. Mater. Chem., 2012, **22**, 6575.

[42] S.C. Sahu, A.K. Samantara, B. Satpati, S. Bhattacharjee and B.K. Jena, Nanoscale**,** 2013, **5**, 11265.

[43] M.B. Gholivand, N. Karimian and M. Torkashvand, J. Anal. Chem., 2015, **70**, 384.

[44] S. Wu, Q. He, C. Tan, Y. Wang and H. Zhang, Small, 2013, **9**, 1160.

[45] A. Ambrosi , C.K. Chua , A. Bonanni , and M. Pumera, Chem. Rev., 2014, **114,** 7150.

[46] C. Huang, C. Li and G. Shi, Energy Environ. Sci.**,** 2012, **5**, 8848.

[47] X. Gan and H. Zhao, Sensors and Materials, 2015, **27**, 191.

[48] L. Li, L. Hu, J. Li and Z. Wei, Nano Research, 2015, **8**, 418.

[49] M. Liu, R. Zhang, and W. Chen, Chem. Rev., 2014, **114**, 5117.

[50] C. Hu, C. Yu, M. Li, X. Wang, Q. Dong, G. Wang and J. Qiu, Chem. Commun.**,** 2015, **51**, 3419.

[51] N.G. Sahoo, Y. Pan, L. Li and S.H. Chan, Advanced Materials, 2012, **24**, 4203.

[52] S. Bong, Y.R. Kim, I. Kim, S. Woo, S. Uhm, J. Lee and H. Kim, Electrochem. Commun. 2010, **12**, 129.

[53] B.F. Machado and P. Serp, Catal. Sci. Technol., 2012, **2**, 54.

[54] X. Huang, X. Qi, F. Boey and H. Zhang, Chem. Soc. Rev.**,** 2012, **41**, 666.

[55] B. Habibi and N. Delnavaz, Int. J. Hydrogen Energy, 2011, **36**, 9581.

[56] B. Habibi and S. Ghaderi, Int. J. Hydrogen Energy, 2015, **40**, 5115.

[57] B. Habibi and N. Delnavaz, RSC Advances, 2012, **2**, 1609.

[58] B. Habibi and S. Dadashpour, Electrochimica. Acta, 2013, **88**, 157.

[59] W.S. Hummers Jr. and R.E. Offeman, J. Am. Chem. Soc., 1958, **80**, 1339.

[60] D.J. Guo, S.K. Cui and H. Sun, J. Nanopart. Res., 2009, **11**, 707.

[61] C.L. Campos, C. Roldán, M. Aponte, Y. Ishikawa and C.R. Cabrera, J. Electroanal. Chem., 2005, **581**, 206.

[62] M. Zhou, N.R. Tacconi and K. Rajeshwar, J. Electroanal. Chem., 1997, **421**, 111.

[63] N.A. Kotov, I. Dekany and J.H. Fendler, Adv. Mater., 1996, **8**, 637.

[64] L. Chen, Y. Tang, K. Wang, C. Liu and S. Luo, Electrochem. Commun., 2011, **13**, 133.

[65] R. Mohammad-Rezaei and H. Razmi, Electroanalysis, 2012, **24**, 2094.

[66] L. Stobinski, B. Lesiak, A. Malolepszy, M. Mazurkiewicz, B. Mierzwa, J. Zemek, P. Jiricek and I. Bieloshapka, J. Electron Spectrosc., 2014, **195**, 145.

[67] F. Li, Y. Guo, T. Wu, Y. Liu, W. Wang and J. Gao, Electrochim. Acta, 2013, **111**, 614.

[68] S. Yu, Q. Liu, W. Yang, K. Han, Z. Wang and H. Zhu, Electrochim. Acta, 2013, **94**, 245.

[69] B.D. Cullity, Addison-Wesley 1978.

[70] J. Zhao, W. Chen and Y. Zheng, Mater. Chem. Phys., 2009, **113**, 591.

[71] S. Trasatti and O.A. Petrii, Pure Appl. Chem., 1991, **63**, 711.

[72] F. Gloaguen, J.M. Leger and C. Lamy, J. Appl. Electrochem., 1997, **27**, 1052.

[73] L.J. Zhang, Z.Y. Wang and D.G. Xia, J. Alloys Compd., 2006, **426**, 268.

[74] J.H. Chen, M.Y. Wang, B. Liu, Z. Fan, K.Z. Cui and Y.F. Kuang, J. Phys. Chem. B, 2006, **110**, 11775.

[75] J. Kua and W.A. Goddard III, J. Am. Chem. Soc., 1999, **121**, 10928.

[76] D.J. Díaz, N. Greenletch, A. Solanki, A. Karakoti and S. Seal, Catal. Lett., 2007,**119**, 319.

[77] A. Hamnet, Catal. Today, 1997, 38, 445.

[78] A. Ciftci, D.A.J.M. Ligthart, P. Pastorino and E.J.M. Hensen, Appl. Catal. B: Environ, 2013, **130**, 325.

[79] B. Habibi and N. Delnavaz, Int. J. Hydrogen Energy, 2010, **35**, 8831.

[80] D. Sebastián, J.C. Calderón, J.A. González-Expósito, E. Pastor, M.V. Martínez-Huerta, I. Suelves, R. Moliner and M.J. Lázaro, Int. J. Hydrogen Energy, 2010, **35**, 9934.

[81] A. Deshpande and N.M. Gupta, Int. J. Hydrogen Energy, 2010, **35**, 3287.

[82] N.P. Sardesai, A. Karimi and S. Andreescu, Chem. Electro. Chem., 2014, **1**, 2082.

[83] T. Masuda, H. Fukumitsu, K. Fugane, H. Togasaki, D. Matsumura, K. Tamura, Y. Nishihata, H. Yoshikawa, K. Kobayashi, T. Mori and K. Uosaki, J. Phys. Chem. C, 2012, **116**, 10098.

[84] L. Feng, J. Yang, Y. Hu, J. Zhu, C. Liu and W. Xing, Int. J. Hydrogen Energy, 2012, **37**, 4812.

[85] A.N. Correia, L.H. Mascaro, S.A.S. Machad and L.A. Avaca, J. Braz. Chem. Soc., 1999, **10**, 478.

[86] Q. Yi, J. Zhang, A.Chen, X. Liu, G. Xu and Z. Zhou, J. Appl. Electrochem., 2008, **38**, 695.

[87] Y.C. Bai, W.D. Zhang, C.H. Chen and J.Q. Zhang, J. Alloys Comp., 2011, **509** 1029.

[88] Z. Wang and K. Qiu, Electrochem. Commun., 2006, **8,** 1075.

[89] Q. Yi, W. Huang, X. Liu, G. Xu, Z. Zhou and A. Chen, J. Electroanal. Chem., 2008, **619-620**, 197.

[90] S. Uhm, H. Jeon and J. Lee, J. Electrochem. Sci.Tech., 2010, **1**, 10.

[91] S. Chakraborty and C.R. Raj, Carbon, 2010, **48**, 3242 .

[92] N. Kristian, Y. Yan and X. Wang, Chem. Commun., 2008, **353-355**, 353.

[93] Q. Yi, A. Chen, W. Huang, J. Zhang, X. Liu,G. Xu and Z. Zhou, Electrochem. Commun., 2007, **9,** 1513.

[94] J. B. Xu, T. S. Zhao and Z. X. Liang, J. Phys. Chem. C, 2008**, 112**, 17362.

[95] V. Selvaraj, M. Alagar and K.S. Kumar, Appl. Catal. B: Environ., 2007, **75** 129.

[96] R. Xie, M. Chen, J. Wang, S. Mei, Y. Pan and H. Gu, RSC Adv., 2015, **5**, 650.

[97] T. Maiyalagan, X. Wang and A. Manthiram, RSC Adv., 2014, **4**, 4028.

[98] V. Selvaraj, A. Nirmala Grace, and M. Alagar, J. Colloid Interf. Sci., 2009, **333**, 254.

[99] A. Nozad Golikand, M. Ghannadi Maragheh, S. Sedaghat Sherehjini, K.M. Taghi-Ganji and M. Yari, Electroanalysis, 2006, **18**, 911.

[100] H. Razmi, Es. Habibi and H. Heidari, Electrochim. Acta, 2008, **53**, 8178.

Legend of Figures:

Fig. 1. CVs (2-8th cycles) showing the electrochemical reduction of graphene oxide (1.0 mg mL^{-1}) in phosphate buffer solution (0.07 M, pH 8.5) on the CCE surface at 20 mV s^{-1}. Inset is the CV of CCE in the same solution without graphene oxide.

Fig. 2. SEM images of CCE (A), RGO/CCE (B), Pt-CeO_2/RGO/CCE (C), Pt-CeO_2/CCE (D), Pt/RGO/CCE (E) and CeO_2/RGO/CCE (F).

Fig. 3. EDX data for Pt-CeO_2/RGO/CCE and EDX data for Pt/RGO/CCE (inset a), CeO_2/RGO/CCE (inset b) and RGO/CCE (inset c).

Fig. 4. XRD patterns of the Pt/RGO/CCE (A) and Pt-CeO_2/RGO/CCE (B).

Fig. 5. CVs of Pt-CeO_2/RGO/CCE (black line) and Pt-CeO_2/CCE (dashed line) in 0.1 M H_2SO_4 at a scan rate of 50 mV s^{-1}.

Fig. 6. CV of 0.1 M formic acid on the Pt-CeO_2/RGO/CCE in 0.1 M H_2SO_4 at a scan rate of 50 mV s^{-1}. Insets are the CVs of Pt-CeO_2/CCE (A), Pt/RGO/CCE (B), Pt/CCE (C), CeO_2/RGO/CCE and RGO/CCE (D, curve1 and 2 respectively) in the same conditions.

Fig. 7. CV of 0.1 M formaldehyde on the Pt-CeO_2/RGO/CCE in 0.1 M H_2SO_4 at a scan rate of 50 mV s^{-1}. Insets are the CVs of Pt-CeO_2/CCE (A), Pt/RGO/CCE (B), Pt/CCE (C), CeO_2/RGO/CCE and RGO/CCE (D, curve1 and 2 respectively) in the same conditions.

Fig. 8. Effect of scan rate on the electrooxidation of 0.1 M formic acid (A) and 0.1 M formaldehyde (B) obtained in 0.1 M H_2SO_4 using Pt-CeO_2/RGO/CCE. Insets (I and I') are the dependence of the anodic peak current densities in the forward scan on the square root of scan rates, (II and II') Variation of anodic peak potentials in forward scan (a_1, a'_1), backward scan (a_2, a'_2) and reduction peak (c_1, c'_1) vs. the square root of scan rates.

Fig. 9. Chronoamperometric curves of 0.1 M formic acid (A) and 0.1 M formaldehyde (B) electrooxidation in 0.1 M H_2SO_4 at the Pt-CeO_2/CCE and Pt-CeO_2/RGO/CCE, respectively.

Fig. 10. Long-term stability of Pt-CeO_2/RGO/CCE in 0.1 M H_2SO_4 and 0.1 M formic acid (A) and 0.1 M formaldehyde (B) vs. number of scans (scan rate 50 mV s^{-1}).

Table captions:

Table 1: Electrochemical parameters of formic acid and formaldehyde electrooxidation on the present electrocatalysts.

Table 2. Comparison of the electrocatalytic performances of the different electrocatalysts toward formic acid and formaldehyde oxidation.

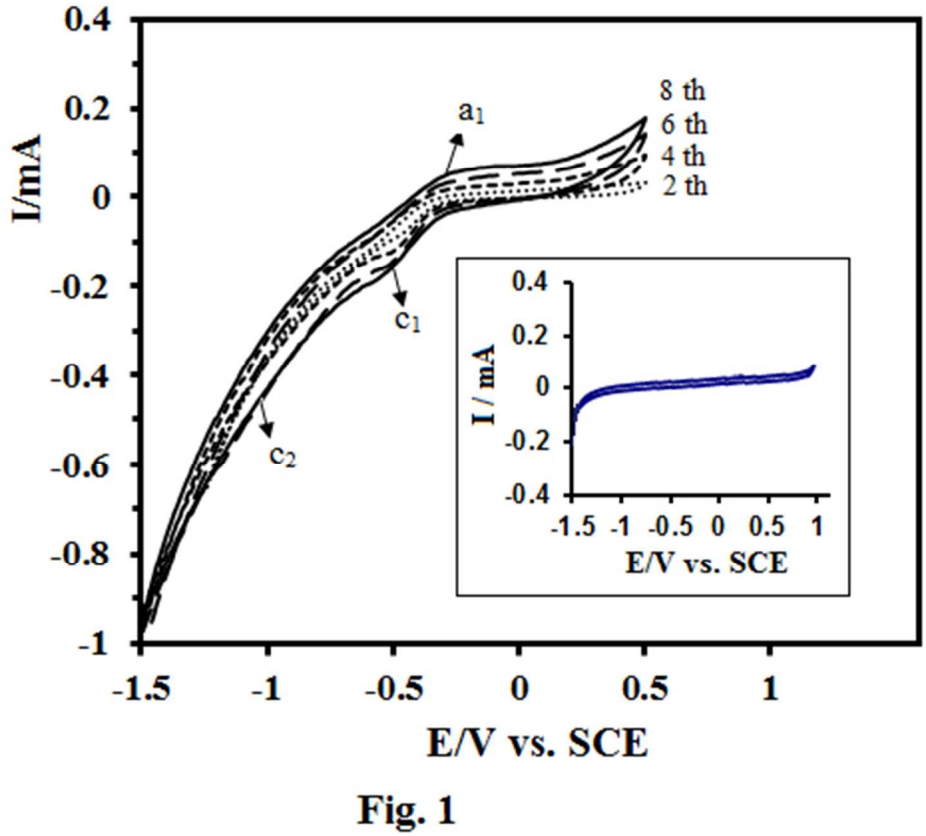

Fig. 1

Fig. 1. CVs (2-8th cycles) showing the electrochemical reduction of graphene oxide (1.0 mg mL-1) in phosphate buffer solution (0.07 M, pH 8.5) on the CCE surface at 20 mV s-1. Inset is the CV of CCE in the same solution without graphene oxide.
133x117mm (96 x 96 DPI)

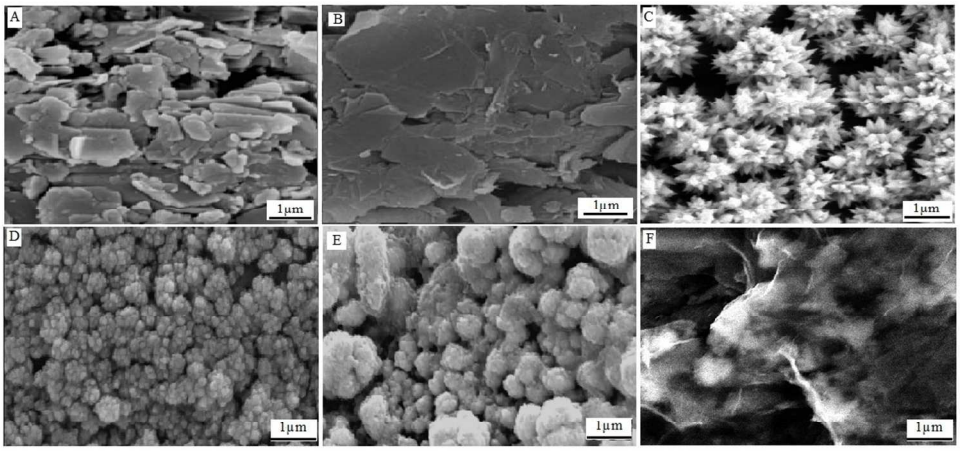

Fig. 2

Fig. 2. SEM images of CCE (A), RGO/CCE (B), Pt-CeO2/RGO/CCE (C), Pt-CeO2/CCE (D), Pt/RGO/CCE (E) and CeO2/RGO/CCE (F).
326x173mm (96 x 96 DPI)

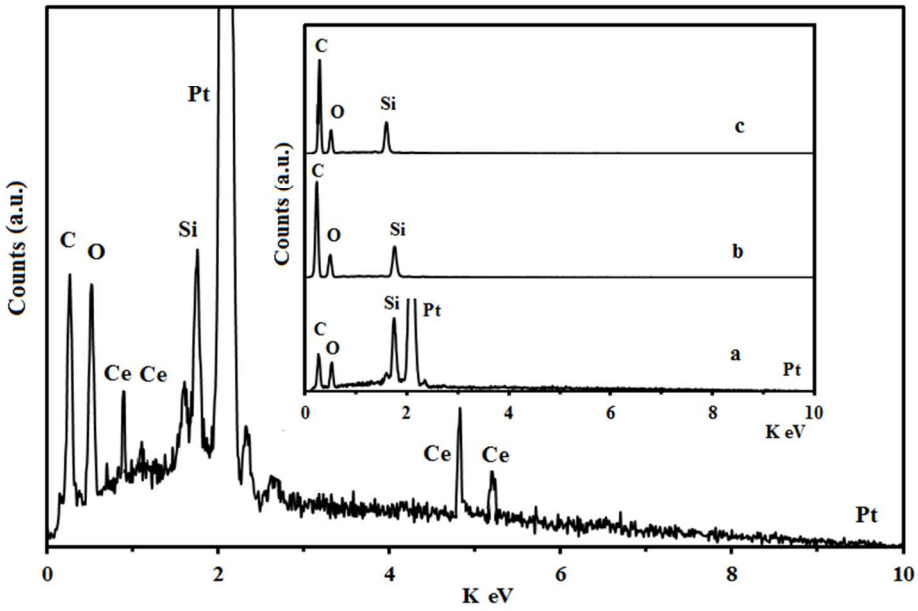

Fig. 3

Fig. 3. EDX data for Pt-CeO2/RGO/CCE and EDX data for Pt/RGO/CCE (inset a), CeO2/RGO/CCE (inset b) and RGO/CCE (inset c).
223x158mm (96 x 96 DPI)

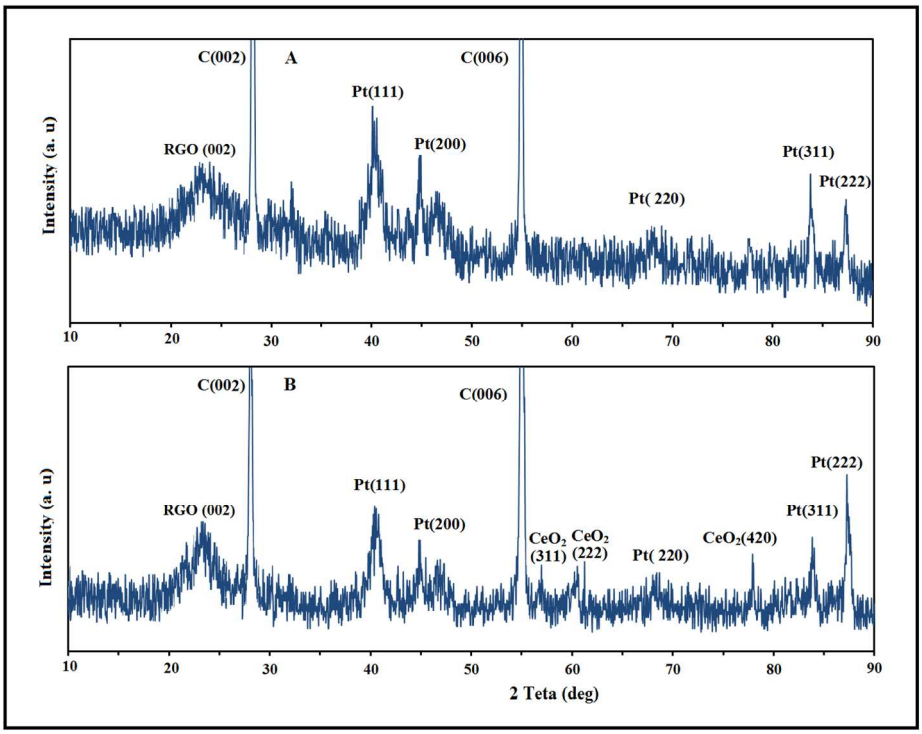

Fig. 4

Fig. 4. XRD patterns of the Pt/RGO/CCE (A) and Pt-CeO2/RGO/CCE (B
411x346mm (96 x 96 DPI)

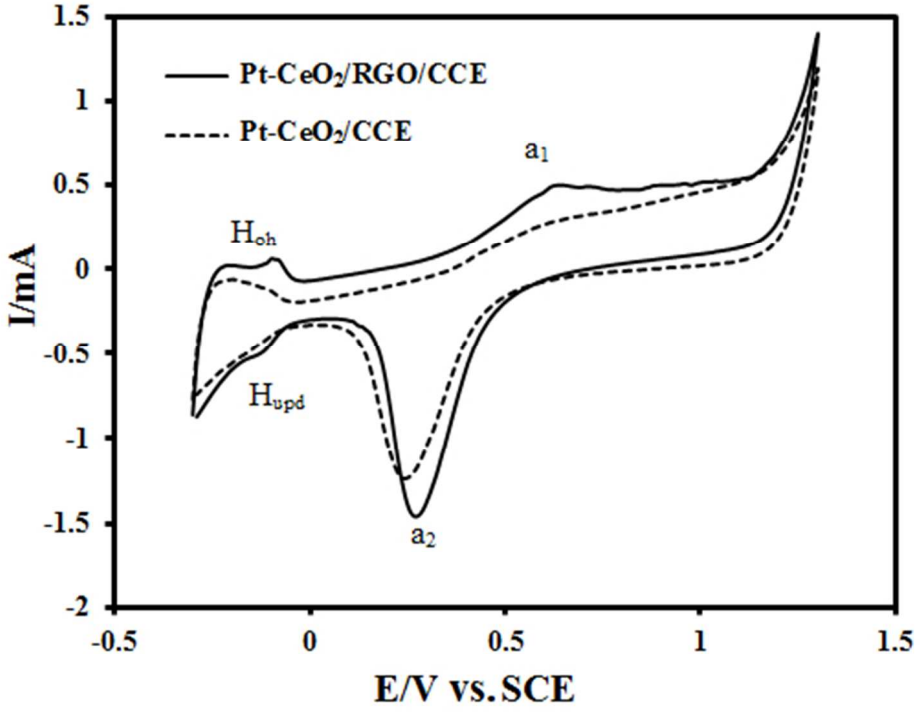

Fig. 5

Fig. 5. CVs of Pt-CeO2/RGO/CCE (black line) and Pt-CeO2/CCE (dashed line) in 0.1 M H2SO4 at a scan rate of 50 mV s-1.
144x133mm (96 x 96 DPI)

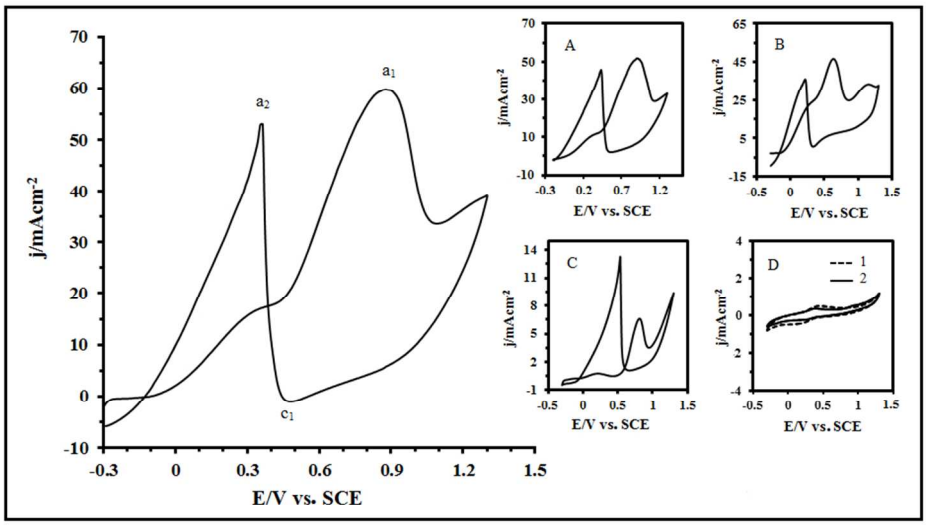

Fig. 6

Fig. 6. CV of 0.1 M formic acid on the Pt-CeO2/RGO/CCE in 0.1 M H2SO4 at a scan rate of 50 mV s-1. The insets are CVs of Pt-CeO2/CCE (A), Pt/RGO/CCE (B), Pt/CCE (C), CeO2/RGO/CCE and RGO/CCE (D, curve1 and 2 respectively) in the same conditions.
268x166mm (96 x 96 DPI)

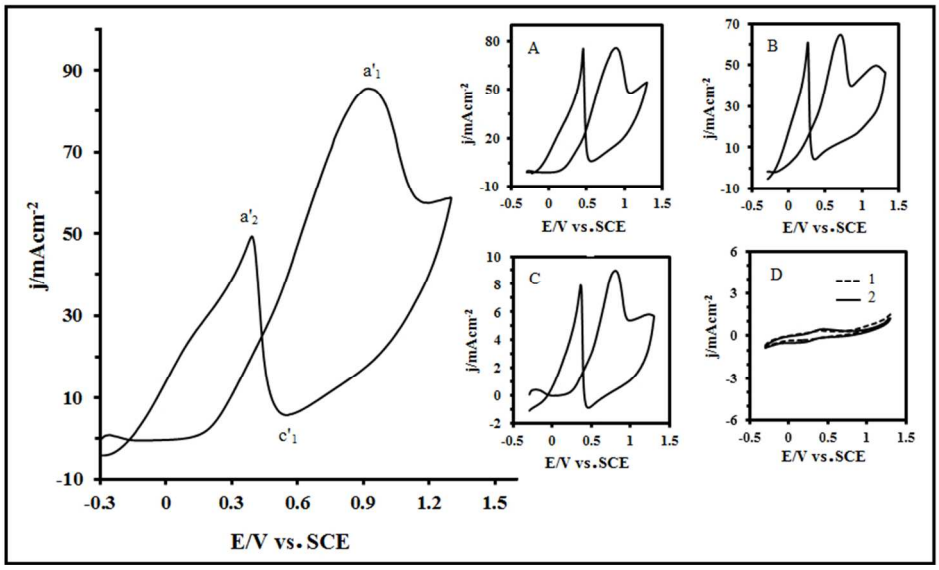

Fig. 7

Fig. 7. CV of 0.1 M formaldehyde on the Pt-CeO2/RGO/CCE in 0.1 M H2SO4 at a scan rate of 50 mV s-1. The insets are CVs of Pt-CeO2/CCE (A), Pt/RGO/CCE (B), Pt/CCE (C), CeO2/RGO/CCE and RGO/CCE (D, curve1 and 2 respectively) in the same conditions.
247x162mm (96 x 96 DPI)

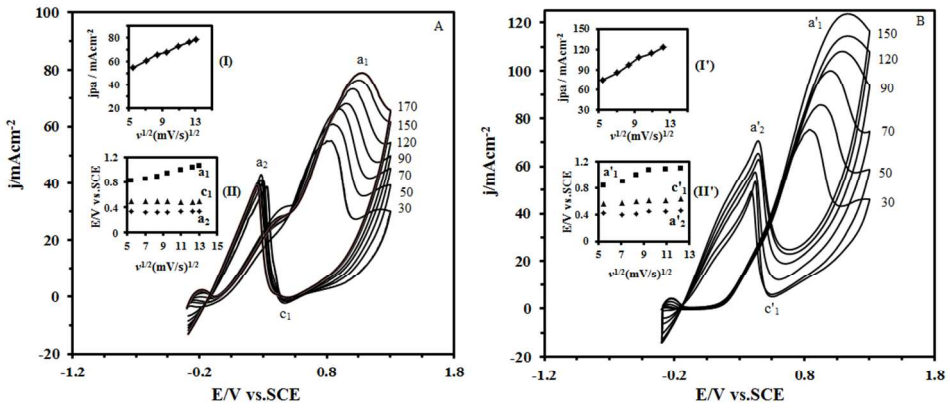

Fig. 8

Fig. 8. Effect of scan rate on the electrooxidation of 0.1 M formic acid (A) and 0.1 M formaldehyde (B) obtained in 0.1 M H2SO4 using Pt-CeO2/RGO/CCE. Insets (I and I') are the dependence of the anodic peak current densities in the forward scan on the square root of scan rates, (II and II') Variation of anodic peak potentials in forward scan (a1, a'1), backward scan (a2, a'2) and reduction peak (c1, c'1) vs. the square root of scan rates.
315x150mm (96 x 96 DPI)

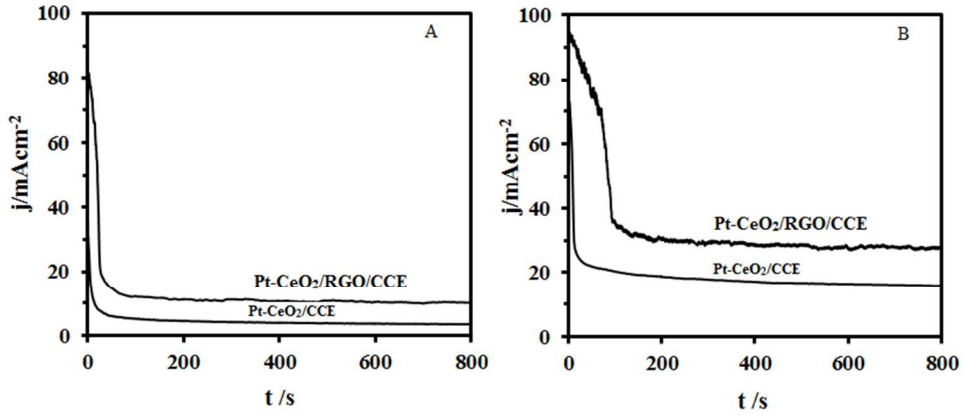

Fig. 9

Fig. 9. Chronoamperometric curves of 0.1 M formic acid (A) and 0.1 M formaldehyde (B) electrooxidation in 0.1 M H2SO4 at the Pt-CeO2/CCE and Pt-CeO2/RGO/CCE, respectively.
228x116mm (96 x 96 DPI)

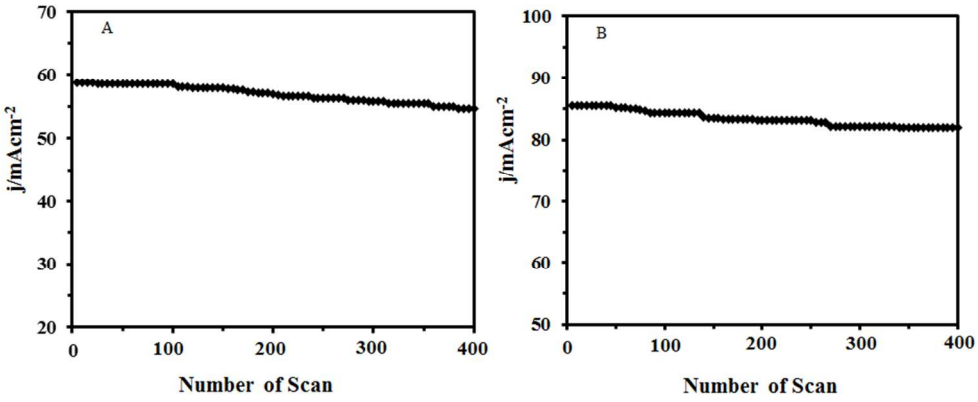

Fig. 10

Fig. 10. Long-term stability of Pt-CeO2/RGO/CCE in 0.1 M H2SO4 and 0.1 M formic acid (A) and 0.1 M formaldehyde (B) vs. number of scans (scan rate 50 mV s-1).
254x120mm (96 x 96 DPI)

Table 1. Electrochemical parameters of formic acid and formaldehyde electrooxidation on the present electrocatalysts.

Fuel	Electrocatalyst	E_{Onset} (V)	E_{pf} (V)	J_{pf} (mA cm^{-2})	E_{pb} (V)	J_{pb} (mA cm^{-2})	J_{pf}/J_{pb}
Formic acid	Pt-CeO_2/RGO/CCE	-0.20	0.87	60	0.36	52.96	1.14
	Pt-CeO_2/CCE	-0.03	0.91	51.8	0.43	45.71	1.13
	Pt/RGO/CCE	-0.11	0.61	46.2	0.21	35.28	1.31
	Pt/CCE	0.0	0.81	6.60	0.53	13.3	0.49
Formaldehyde	Pt-CeO_2/RGO/CCE	0.07	0.92	85.58	0.39	49.26	1.73
	Pt-CeO_2/CCE	0.13	0.88	75.90	0.45	75.16	1.01
	Pt/RGO/CCE	-0.21	0.64	61.6	0.25	59.65	1.03
	Pt/CCE	0.09	0.81	8.98	0.36	7.92	1.13

Table 2. Comparison of the electrocatalytic performances of the different electrocatalysts toward formic acid and formaldehyde oxidation.

Electrocatalyst	Fuel	E_{onset} (SCE)	E_{pf}	E_{pb}	J_{pf} [a]	J_{pb}	J_{pf}/J_{pb}	Stab.[c]	Ref.
Pt-Au/graphene electrode	formic acid	-104	710	466	0.621(A/mg) peak (II)(1M)[b]	2.7(A/mg)	0.23	3h	23
	formaldehyde	-	-	-	-	-	-	-	
Pt-Ni/CCE	formic acid	-150	800	380	1.82 mA/cm^2 S_{Real} (0.5M)	1.82 mA/cm^2	1	1.1h	55
	formaldehyde	-	-	-	-	-	-	-	
Pt-Sn/CCE	formic acid	-0.3	690	290	1.3 mA (0.5M)	1.23 mA 0.5M)	1.05	-	57
	formaldehyde	-	-	-	-	-	-	-	
Pt/CCE	formic acid	-100	810	540	49.43 mA/cm^2 S_{Geo} (0.75M)	103.6 mA/cm^2	0.47	0.14h	79
	formaldehyde	140	820	370	65.57 mA/cm^2 S_{Geo} (0.75M)	57.14 mA/cm^2	1.14	0.14h	
Pd-Si alloy	formic acid	-	671	281	0.35 mA/cm^2 (0.5M)	0.8 mA/cm^2	0.44		85
	formaldehyde	-	756	556	1.65 mA/cm^2 (0.5M)	2.75 mA/cm^2	0.6	-	
nanoPtSn/Ti	formic acid		725	500	13.75 mA/cm^2 S_{Geo} (0.5M)	31.25 mA/cm^2	0.44	0.23h	86
	formaldehyde	-	-	-	-	-	-	-	
PtAu/MWCNTs	formic acid	-50	705	555	2.5 mA/cm^2 S_{Real} (0.5M)	7.2 mA/cm^2	0.35	0.7 h	87
	formaldehyde	-	-	-	-	-	-	-	
PtNPs/ nichrome	formic acid	100	730	545	6.5 mA	5.5 mA	1.18	-	88
	formaldehyde	-	-	-	-	-	-	-	
Pt50Pd50/Ti	formic acid	-100	700	400	28 mA/cm^2 (0.5M)	110 mA/cm^2	0.26	0.22	89
	formaldehyde	-	-	-	-	-	-	-	
AuPt(7:3)/ carbon paper	formic acid	-45	558	735	87.5 mA/cm^2 (0.5M)	125 mA/cm^2	0.7	3.16h	90
	formaldehyde	-	-	-	-	-	-	-	
nPd on the MWCNT electrode	formic acid	-244	406	436	1.935 mA (0.1 M)	2.750	0.7	-	91
	formaldehyde	-	-	-	-	-	-	-	
PtAu/C (core–Shell)	formic acid		700	330	0.91 mA (0.5 M)	2.65 mA	0.34	-	92
	formaldehyde	-	-	-	-	-	-	-	
Nano Pt59Ir41/Ti	formic acid	0	750	500	100 mA/cm^2 (0.5M)	253 mA/cm^2	0.4	0.2 h	93
	formaldehyde	-	-	-	-	-	-	-	
PtAg/C	formic acid	0	680	430	33 mA/cm^2 S_{Geo} (0.5M)	69 mA/cm^2	0.48		94
	formaldehyde	-	-	-	-	-	-	-	
Pt-Pd nanoparticles/PPy-CNT-GEs	formic acid	0	650	370	30 mA/cm^2 S_{Geo} (0.5M)	41.25 mA/cm^2	0.72	0.34 h	95
	formaldehyde	140	590	380	38.5 mA/cm^2 S_{Geo} (0.5M)	45.5 mA/cm^2	0.85	0.34 h	
Au-Pt NCs	formic acid	-100	660	400	666.67 (mA mg^{-1} Pt) 0.5M)	1772(mA mg^{-1} Pt)	0.38	0.25h	96
	formaldehyde	-	-	-	-	-	-	-	
Pd-Au (3 : 1)/PDDA-xGNP	formic acid	-	445	252	480(mA mg^{-1} Pd) (0.5M)	580 (mA mg^{-1} Pd)	0.83	1 h	97
	formaldehyde	-	-	-	-	-	-	-	
Pt-Pd/SWCNT	formic acid	10	680	300	28.26 mA/cm^2	29.93	0.94	0.17 h	98

					(0.5M)	mA/cm^2			
	formaldehyde	200	600	380	33.56 mA/cm^2 (0.5M)	18.05 mA/cm^2	1.86	0.17h	
Pt-CeO_2 /RGO/CCE	formic acid	-200	870	360	60 mA/cm^2 S_{Geo} (0.1M)	52.96 mA/cm^2	1.14	0.22 h	This work
	formaldehyde	70	920	390	85.58 mA/cm^2 S_{Geo} (0.1M)	49.26 mA/cm^2	1.73	0.22 h	

[a] S_{Geo}= based on geometric surface area and S_{Real} based real surface area.
[b] Fuel concentration.
[c] Stability based on reported chronoamperometric curves.